mice via the tail vein on days 0 and 4. Mice were sacrificed on day 6, and the tumors were excised, frozen in dry-iced acetone, and sectioned at 10 μm thickness in a cryostat. Vascular endothelial cells (VECs) were immunostained by rat monoclonal antibody antiplatelet endothelial cell adhesion molecule-1 (PECAM-1) (BD Pharmingen, Franklin Lakes, NJ) and Alexa488-conjugated secondary antibody. The samples were observed with a confocal laser scanning microscope (CLSM). The CLSM observation was performed using an LSM 510 (Carl Zeiss, Oberlochen, Germany) with an EC Plan-Neoflur 20× objective (Carl Zeiss) at the excitation wavelength of 488 nm (Ar laser). The PECAM-1-positive area (%) was calculated from Alexa488-positive pixels.

***In Vivo* EGFP Gene Expression in the Tumors.** Polyplex micelles loading EGFP pDNA (20 μg of pDNA) were injected into the BxPC3-inoculated mice via the tail vein. Mice were sacrificed on either day 3 or day 7. Tumors were excised, fixed with 10% formalin, frozen, and sectioned. VECs were immunostained by anti-PECAM-1 antibody and Alexa647-conjugated secondary antibody. After nuclear staining with Hoechst 33342, CLSM observation was carried out using the LSM 510 with the EC Plan-Neoflur 20× objective at the excitation wavelength of 488 nm for EGFP expression, 633 nm (He−Ne laser) for Alexa647, and 710 nm (MaiTai laser, two photon excitation; Spectra-Physics, Mountain View, CA) for Hoechst 33342, respectively. The representative images of tumors excised on day 3 are shown in Figure 5. Note that images of tumors excised on day 7 showed similar patterns to those on day 3, however with lower intensity of EGFP expression.

Results

Formation of Polyplex Micelles. No free pDNA was detected by agarose gel electrophoresis, confirming that all pDNA was entrapped in disulfide cross-linked polyplex micelles, which were prepared as previously reported through ion complexation of block copolymers with pDNA at the N/P ratio = 2. Free thiol groups in polyplex micelles were estimated to be less than 2% by Ellman's test (data not shown), which is consistent with our previous report.[10] Weight−weight % ratios of pDNA/micelle in each formulation were as follows: 32.8% in B-SH0% formulation; 31.0% in B-SH5%; 29.2% in B-SH11%; 26.4% in B-SH20%; and 21.0% in B-SH36%. The mean size of the micelles was between 100 and 150 nm, with a moderate polydispersity index between 0.17 and 0.2 (Figure 3 in the Supporting Information), while zeta-potential revealed approximately neutral values, confirming the formation of PEG palisade surrounding the polyplex core (Table 1).

Real-Time Gene Expression. *In vitro* real-time Luc gene expression of polyplex micelles was evaluated using Kronos Dio for a prolonged period (Figure 1).[17,18] The B-SH5% cross-linked polyplex micelle showed the highest gene expression among all micelles until 60 h. Worth mentioning is that the transfection efficiency of the B-SH11% micelle continued to exceed that of the B-SH5% micelle after 60 h. Disulfide cross-links in the polyplex core are believed to contribute not only to enhanced stability of the micelles in the medium but also to sustained release of complexed pDNA inside the cells with a reductive environment, resulting in polyplex micelles with higher cross-linking rates that can maintain an appreciable transfection efficiency over a longer time scale. Note that the B-SH36% micelle showed an increasing trend in gene expression with time.

Antitumor Activity. Polyplex micelles containing sFlt-1 pDNA were injected iv into mice bearing pancreatic adenocarcinoma BxPC3, followed by evaluation of tumor volume (Figure 2). All the micelles were injected three times on days

Table 1. Sizes and Zeta-Potentials of Polyplex Micelles with Various Cross-Linking Rates at N/P = 2[a]

thiolation degree (%)	cumulant diameter (nm)	polydispersity index (μ/T^2)	zeta-potential (mV)
0	107 ± 2	0.195 ± 0.021	1.66 ± 0.28
5	117 ± 2	0.184 ± 0.011	1.25 ± 0.40
11	116 ± 2	0.171 ± 0.013	1.02 ± 0.30
20	139 ± 6	0.182 ± 0.050	0.40 ± 0.07
36	147 ± 2	0.192 ± 0.061	−0.96 ± 0.02

[a] The results reported were expressed as mean ± SEM (n = 3).

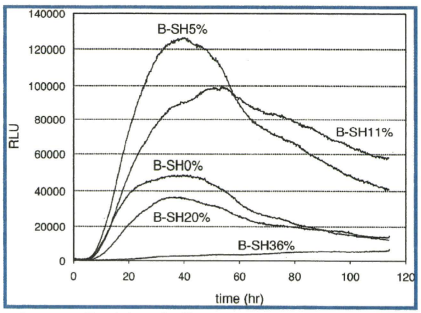

Figure 1. Real-time luciferase gene expression of the polyplex micelles with varying thiolation degrees at N/P = 2 against 293T cells.

(17) Takae, S.; Miyata, K.; Oba, M.; Ishii, T.; Nishiyama, N.; Itaka, K.; Yamasaki, Y.; Koyama, H.; Kataoka, K. PEG-detachable Polyplex Micelles Based on Disulfide-crosslinked Block Catiomers as Bioresponsive Nonviral Gene Vectors. *J. Am. Chem. Soc.* **2008**, *130*, 6001–6009.

(18) Oba, M.; Aoyagi, K.; Miyata, K.; Matsumoto, Y.; Itaka, K.; Nishiyama, N.; Yamasaki, Y.; Koyama, H.; Kataoka, K. Polyplex Micelles with Cyclic RGD Peptide Ligands and Disulfide Cross-links Directing to the Enhanced Transfection via Controlled Intracellular Trafficking. *Mol. Pharmaceutics* **2008**, *5*, 1080–1092.

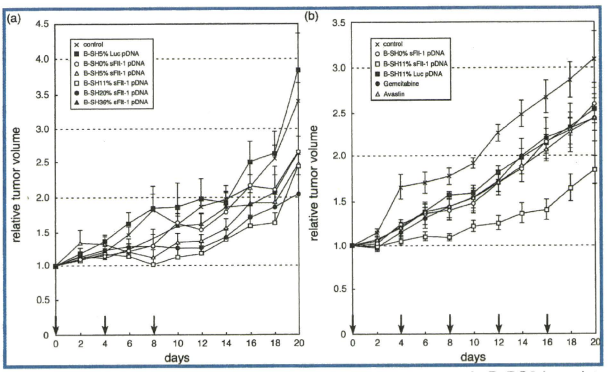

Figure 2. Antitumor activity of polyplex micelles with sFlt-1 pDNA in subcutaneously BxPC3-inoculated mice. (a) Effect of thiolation degree. Hepes buffer (control) was used as a negative control. Polyplex micelles were injected iv on days 0, 4, and 8 at 20 μg pDNA/mouse, and mice were monitored for the relative tumor volume every second day. Error bars represent the SEM ($n = 6$). Only the B-SH11% polyplex micelles exhibited significant retardation of tumor growth compared to the control ($P < 0.01$). (b) Growth curve study with an increased dose of the B-SH11% polyplex micelles compared to commercially available drugs. Polyplex micelles (20 μg pDNA/mouse), gemcitabine (100 mg/kg), and Avastin (50 mg/kg) were injected iv on days 0, 4, 8, 12, and 16. Relative tumor size was measured every second day. Hepes buffer (control) was used as a negative control. Error bars represent the SEM ($n = 5$). Only the B-SH11% polyplex micelles exhibited significant retardation of tumor growth compared to the control ($P < 0.001$). P values were calculated by multivariate ANOVA study.

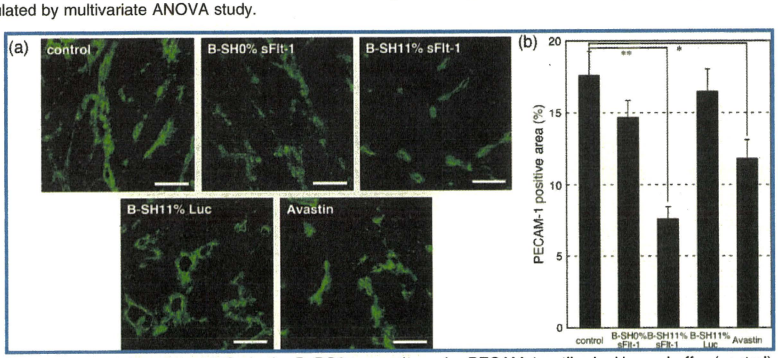

Figure 3. Immunostaining of the VECs in the BxPC3 tumor tissue by PECAM-1 antibody. Hepes buffer (control), three types of polyplex micelles (20 μg of pDNA/mouse), and Avastin (50 mg/kg) were injected into the BxPC3-inoculated mice via the tail vein on days 0 and 4. Mice were sacrificed on day 6, and tumors were excised and immunostained. (a) CLSM images of immunostained tumors. PECAM-1-positive regions are green. Bars represent 100 μm. (b) Areas of PECM-1-positive endothelium were quantified. Error bars represent the SEM ($n = 15$). P values were calculated by Student's t test. $^*P < 0.01$ and $^{**}P < 0.001$.

0, 4, and 8 (Figure 2a). The B-SH11% micelle significantly suppressed tumor growth compared to control mice treated with Hepes buffer ($P < 0.01$). There was no significant change in tumor growth after injection of other polyplex micelles, implying that an optimal cross-linking rate is required to achieve an effective expression of the gene. Encouraged by these results, the tumor growth suppression activity of B-SH11% micelle was further evaluated, implying a regimen with enhanced number of injections. The effect of the micelles was compared to commercially available drugs, gemcitabine, a standard chemotherapeutic agent for pancreatic tumor, and bevacizumab (Avastin), a monoclonal antibody against VEGF (Figure 2b). The doses of gemcitabine and Avastin implied in our study were based on

previous reports published elsewhere.[15,16] The administration of B-SH11%/sFlt-1 micelle resulted in significant suppression of tumor growth ($P < 0.001$), while gemcitabine and Avastin, under the reported experimental regimen, showed no remarkable therapeutic effect. Note that the difference observed in tumor volumes between the B-SH11%/Luc micelle-treated group and the control group was not significant.

Tumor Vascular Density. The antiangiogenic effect of expressed sFlt-1 was confirmed by immunostaining of VECs using PECAM-1 (Figure 3). Vascular density of tumors treated with either B-SH11%/sFlt-1 micelle or Avastin was significantly lower than that of the other groups. The most pronounced and significant effect on neo-vasculature suppression was achieved by B-SH11%/sFlt-1 micelle (7% PECAM-1 positive area) over Avastin (12% PECAM-1 positive area) ($P < 0.05$). These results suggest that the expressed sFlt-1 may entrap VEGF secreted in the tumor tissue, thereby suppressing the growth of VECs.

***In Vivo* sFlt-1 Gene Expression.** Expression levels of sFlt-1 in the body were then evaluated by measuring the amount of sFlt-1 in lung, liver, spleen, kidney, tumor, and blood plasma using enzyme-linked immunosorbent assay (ELISA) (Figure 4). Injection of B-SH11%/sFlt-1 micelle resulted in significantly higher expression of sFlt-1 selectively in tumor tissue compared to the control. On the other hand, injection of B-SH0%/sFlt-1 micelle or B-SH11%/Luc micelle did not result in any difference in sFlt-1 expression compared to the control. These results strongly support that tumor-specific elevation in sFlt-1 expression led to the significant growth suppression of VECs in the tumor tissue and, eventually, the suppression of tumor growth.

***In Vivo* Enhanced Green Fluorescence Protein (EGFP) Gene Expression in Tumors.** The location of gene expression in BxPC3 tumors after administration of the micelles was analyzed histologically using pDNA encoding EGFP (Figure 5). As previously reported,[13,19,20] thick fibrotic tissue was formed around blood vessels (red) inside the stroma of BxPC3 tumors, and nests of tumor cells (region T) were scattered in the stroma (Figure 5a). The expression of EGFP (Figures 5b and 5c) was observed mainly in the VECs and cells in stromal regions adjacent to some vasculature, indicating that VECs and fibroblasts near some vasculature in the stroma, but not the tumor cells, were transfected. As seen in Figure 5a, there were thick fibrotic tissues around blood vessels in the BxPC3 xenograft,

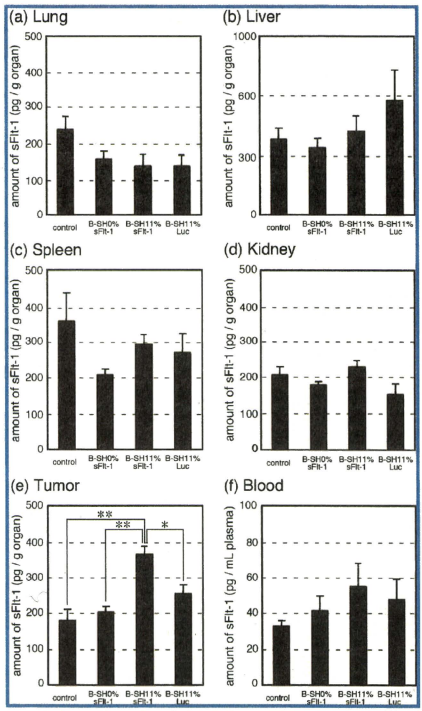

Figure 4. Evaluation of sFlt-1 gene expression in organs by ELISA. Hepes buffer (control) and three types of polyplex micelles (20 μg pDNA/mouse) were injected into the BxPC3-inoculated mice via the tail vein on days 0 and 4. Mice were sacrificed on day 6 after collecting blood (f), and the lungs (a), livers (b), spleens (c), kidneys (d), and tumors (e) were excised, followed by evaluation of sFlt-1 concentration by ELISA according to the manufacturer's protocol. Error bars represent the SEM ($n = 6$). P values were calculated by Student's t test. $^*P < 0.01$ and $^{**}P < 0.001$.

indicating that the penetration of polyplex micelles deep into the stroma or into the tumor nest was interrupted and the gene expression was limited in the VECs and some of the fibroblasts in the stroma. Higher levels of EGFP expression were observed for B-SH11% micelle, confirming their enhanced ability to accumulate inside tumor tissue compared to B-SH0% micelle.

Discussion

Since all solid tumors need angiogenesis for their growth, antiangiogenic therapy is a promising strategy for treating

(19) Miyata, K.; Oba, M.; Kano, M. R.; Fukushima, S.; Vachutinsky, Y.; Han, M.; Koyama, H.; Miyazono, K.; Nishiyama, N.; Kataoka, K. Polyplex Micelles from Triblock Copolymers Composed of Tandemly Aligned Segments with Biocompatible, Endosomal Escaping, and DNA-condensing Functions for Systemic Gene Delivery to Pancreatic Tumor Tissue. *Pharm. Res.* **2008**, *25*, 2924–2936.

(20) Kano, M. R.; Komuta, Y.; Iwata, K.; Oka, M.; Shirai, Y.; Morishita, Y.; Ouchi, Y.; Kataoka, K.; Miyazono, K. Comparison of the Effects of the Kinase Inhibitors Imatinib, Sorafenib, and Transforming Growth Factor-β Receptor Inhibitor on Extravasation of Nanoparticles from Neovasculature. *Cancer Sci.* **2009**, *100*, 173–180.

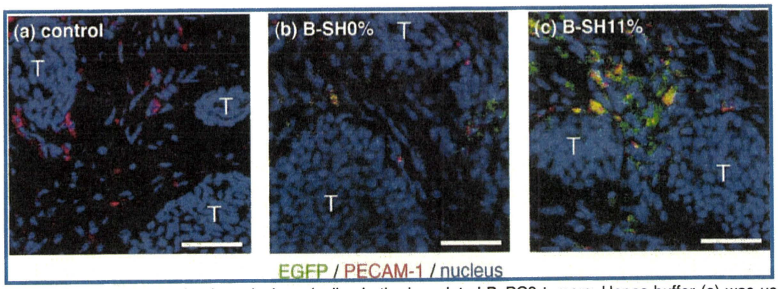

Figure 5. EGFP gene expression by polyplex micelles in the inoculated BxPC3 tumors. Hepes buffer (a) was used as a negative control. B-SH0% (b) and B-SH11% (c) polyplex micelles containing EGFP pDNA (20 μg pDNA/mouse) were injected into the BxPC3-inoculated mice via the tail vein. Mice were sacrificed on day 3, and tumors were excised and immunostained. "T" indicates nests of tumor cells in tumor tissues. Bars represent 50 μm.

tumor patients. In fact, Avastin, the recombinant humanized monoclonal antibody against VEGF, has been widely used as an antiangiogenic drug, and its application range is spreading to the various types of solid tumors.[16] Other antiangiogenic proteins,[21,22] e.g., angiostatin, endostatin, and soluble forms of VEGF receptor, have also received great attention. Meanwhile, antiangiogenic gene therapy represents an attractive alternative to antiangiogenic proteins for reasons such as low dose, continuous expression of the therapeutic protein, and low cost. Therefore, development of an effective and safe gene vector is a key to successful antiangiogenic gene therapy.

In this study, thiolated PEG-PLys block copolymers were applied in the formation of disulfide cross-linked polyplex micelles for delivery of pDNA encoding sFlt-1, and tested for their antiangiogenic effect on mice bearing xenografted BxPC3 cell line, derived from human pancreatic adenocarcinoma. Disulfide cross-links in the polyplex core were designed to increase blood stability of the polyplex micelles and effectively release pDNA in the intracellular milieu.[10,11,18] PEG palisade of the polyplex micelle is expected to cover the polyplex core to shield the positive charge as well as to decrease interfacial free energy.[12,23] The formation of the PEG palisade surrounding the polyplex core was confirmed by the neutral zeta-potential of the polyplex micelles (Table 1). B-SH36% micelle showed an approximately 10 times higher concentration of pDNA in the blood at 60 min after iv injection than that of the micelle without core cross-linking (B-SH0%) (Figure 4 in the Supporting Information). The disulfide cross-links in the polyplex core apparently contribute to the enhanced stability of the micelles in the bloodstream. Note that the size of polyplex micelles is between 100 and 150 nm (Table 1), which may be in a suitable range for accumulation in solid tumors due to the enhanced permeability and retention (EPR) effect,[24] although the size may be too large to allow the micelles to penetrate into the stroma in pancreatic tumors.[13] Nevertheless, there is a concern that excessive disulfide cross-links interfere with the smooth release of entrapped pDNA in the core, resulting in decreased transfection efficiency.[10] Accordingly, optimal cross-linking density should be determined to balance the stability and maintain high transfection efficiency. The results of *in vitro* real-time gene expression showed that B-SH5% micelle possessed the highest efficiency among the evaluated samples up to 60 h after transfection. It is noteworthy that B-SH11% micelle exerted sustained Luc expression and kept an appreciably high efficiency beyond 60 h (Figure 1). Apparently, gene expression is prolonged with an increase in cross-linking rates, although excess cross-links induced overstabilization of polyplex micelles, resulting in decreased transfection efficiency in the case of the B-SH20% and B-SH36% micelles. Eventually, the B-SH36%/sFlt-1 micelle had no *in vivo* efficiency, even though they showed the highest stability in the bloodstream among the evaluated samples (Figure 4 in the Supporting Information). It is also noteworthy that the B-SH11%/sFlt-1 micelle achieved an appreciably high therapeutic efficiency, even though it showed only limited improvement in blood circulation time compared to the B-SH0% and B-SH5% systems. Presumably, a sustained

(21) Sim, B. K. L.; MacDonald, N. J.; Gubish, E. R. Angiostatin and Endostatin: Endogenous Inhibitors of Tumor Growth. *Cancer Metastasis Rev.* **2000**, *19*, 181–190.

(22) Fischer, C.; Mazzone, M.; Jonckx, B.; Carmeliet, P. FLT1 and Its Ligands VEGFB and PIGF: Drug Targets for Anti-angiogenic Therapy. *Nat. Rev. Cancer* **2008**, *8*, 942–956.

(23) Kakizawa, Y.; Kataoka, K. Block Copolymer Micelles for Delivery of Gene and Related Compounds. *Adv. Drug Delivery Rev.* **2002**, *54*, 203–222.

(24) Matsumura, Y.; Maeda, H. A New Concept for Macromolecular Therapeutics in Cancer Chemotherapy: Mechanism of Tumoritropic Accumulation of Proteins and the Antitumor Agent Smancs. *Cancer Res.* **1986**, *46*, 6387–6392.

profile in gene expression may have been the key to this achievement. Note that no change in body weight of the mice was observed during the experiment (data not shown), indicating few serious side effects of polyplex micelles.

Comparison with the commercially available agents, gemcitabine and Avastin, confirmed the encouraging tumor growth suppression effect of the B-SH11% polyplex micelle (Figure 2b). Gemcitabine continues to be the standard therapy in the treatment of pancreatic tumors; however, its objective response rate is limited in patients with advanced disease.[25] Avastin is a recombinant humanized monoclonal antibody against human VEGF, which may neutralize tumor-cell-derived VEGF in the model used here. In humans, Avastin is the first clinically available antiangiogenic drug, and it has been efficient when used in combined chemotherapy for metastatic colorectal cancer[26] and non-small-cell lung cancer.[27] However, it showed no benefit in patients with pancreatic tumors.[25] The B-SH11%/sFlt-1 micelle significantly suppressed tumor growth compared not only to the control ($P < 0.001$) but also to the B-SH11%/Luc micelle, gemcitabine, and Avastin ($P < 0.01$) (Figure 2b). Xenografted BxPC3 was reported not to respond to gemcitabine,[28] probably due to its inability to penetrate through the tumor thick fibrotic tissue and target tumor cells, which is consistent with our results. Evaluation of vascular density in BxPC3 tumor (Figure 3) clearly showed that the B-SH11%/sFlt-1 micelle decreased vascular density compared to the control ($P < 0.001$), the B-SH11%/Luc micelle ($P < 0.001$), and Avastin ($P < 0.05$) treated tumors.

Inhibitory effect on tumor growth (Figure 2) is consistent with the result of decreased vascular density. There are several studies on antiangiogenic gene therapy for subcutaneously inoculated tumors in mice by systemic expression of sFlt-1 using viral vectors, including im injection of adeno-associated viral vectors[29] and iv injection of adenoviral vectors to target livers.[30] In these studies, however, sFlt-1 was expressed mainly in organs rather than tumor tissue. What was worse, the excess expression of sFlt-1 in the liver led to unacceptable hepatotoxicity.[31] Thus, tumor-specific expression of sFlt-1 is essential for a safe and efficient antiangiogenic gene therapy. However, any nonviral gene vectors loading sFlt-1 gene have failed to exhibit selective gene expression in the tumor tissue, although they achieved certain inhibition of tumor growth.[8,9] In this regard, the B-SH11%/sFlt-1 micelle system might be promising, since sFlt-1 expression was significantly increased selectively in the tumor tissue compared not only to the control ($P < 0.001$) but also to the B-SH11%/Luc micelle ($P < 0.01$), as shown in Figure 4, without any significantly enhanced expression in other normal tissues. Note that no significant increase of sFlt-1 expression was observed in any normal organs treated with B-SH0%/sFlt-1 micelle or B-SH11%/Luc micelle. Histological analyses revealed that EGFP expression of the B-SH11%/EGFP micelle was located mainly around VECs but not in the tumor cells (Figure 5), probably due to restricted permeation of micelles by thick fibrotic tissues and pericyte-covered vasculature of the BxPC3 tumors. These results suggested the ability of expressed sFlt-1 molecule to entrap excess VEGF in the tumor tissue and to inhibit tumor growth by an antiangiogenic effect. Xenografted BxPC3 tumors in mice are characterized by stroma-rich histology,[20] which might explain the only slight inhibitory effects on BxPC3 growth achieved by gemecitabine[28] targeting tumor cells.

Conclusions

In conclusion, antiangiogenic gene therapeutic study was carried out by iv administration of polyplex micelles with sFlt-1 pDNA to mice bearing pancreatic adenocarcinoma BxPC3 xenografts, and the results demonstrated the ability of B-SH11% sFlt-1 micelle as a safe and effective gene delivery system. The optimal disulfide cross-linking rate of polyplex micelles was found to show significant suppression of tumor growth. Gene expression of sFlt-1 by iv injection of polyplex micelles was observed in tumor tissue only, followed by decreased vascular density and significant suppression of tumor growth. Based on these results, the B-SH11% disulfide cross-linked polyplex

(25) Rocha-Lima, C. M. New Directions in the Management of Advanced Pancreatic Cancer: a Review. *Anti-Cancer Drugs* **2008**, *19*, 435–446.

(26) Hurwitz, H.; Fehrenbacher, L.; Novotny, W.; Cartwright, T.; Hainsworth, J.; Heim, W.; Berlin, J.; Baron, A.; Griffing, S.; Holmgren, E.; Ferrara, N.; Fyfe, G.; Rogers, B.; Ross, R.; Kabbinavar, F. Bevacizumab Plus Irinotecan, Fluorouracil, and Leucovorin for Metastatic Colorectal Cancer. *N. Engl. J. Med.* **2004**, *350*, 2335–2342.

(27) Sandler, A.; Gray, R.; Perry, M. C.; Brahmer, J.; Schiller, J. H.; Dowlati, A.; Lilenbaum, R.; Johnson, D. H. Paclitaxel-carboplatin Alone or with Bevacizumab for Non-small-cell Lung Cancer. *N. Engl. J. Med.* **2006**, *355*, 2542–2550.

(28) Merriman, R. L.; Hertel, L. W.; Schultz, R. M.; Houghton, P. J.; Houghton, J. A.; Rutherford, P. G.; Tanzer, L. R.; Boder, G. B.; Grindey, G. B. Comparison of the Antitumor Activity of Gemcitabine and Ara-C in a Panel of Human Breast, Colon, Lung and Pancreatic Xenograft Models. *Invest. New Drugs* **1996**, *14*, 243–247.

(29) Takei, Y.; Mizukami, H.; Saga, Y.; Yoshimura, I.; Hasumi, Y.; Takayama, T.; Kohno, T.; Matsushita, T.; Okada, T.; Kume, A.; Suzuki, M.; Ozawa, K. Suppression of Ovarian Cancer by Muscle-Mediated Expression of Soluble VEGFR-1/Flt-1 Using Adeno-associated Virus Serotype 1-derived Vector. *Int. J. Cancer* **2006**, *120*, 278–284.

(30) Liu, J.; Li, J.; Su, C.; Huang, B.; Luo, S. Soluble Fms-like Tyrosine Kinase-1 Expression Inhibits the Growth of Multiple Myeloma in Nude Mice. *Acta Biochim. Biophys. Sin.* **2007**, *39*, 499–506.

(31) Mahasreshti, P. J.; Kataram, M.; Wang, M. H.; Stockard, C. R.; Grizzle, W. E.; Carey, D.; Siegal, G. P.; Haisma, H. J.; Alvarez, R. D.; Curiel, D. T. Intravenous Delivery of Adenovirus-mediated Soluble FLT-1 Results in Liver Toxicity. *Clin. Cancer Res.* **2003**, *9*, 2701–2710.

micelle with sFlt-1 pDNA is interesting and worthy to develop further for antiangiogenic gene therapy of solid tumors.

Acknowledgment. This work was financially supported in part by the Core Research Program for Evolutional Science and Technology (CREST) from Japan Science and Technology Agency (JST) as well as by Grants-in-Aid for Young Scientists (A) and Exploratory Research. We express our appreciation to Masabumi Shibuya (Tokyo Medical and Dental University) for providing pVL 1393 baculovirus vector pDNA encoding human sFlt-1. We thank Kazuhiro Aoyagi, Yoko Hasegawa, Kotoe Date, and Satomi Ogura (The University of Tokyo) for technical assistance.

Supporting Information Available: Synthesis of thiolated block copolymer and Supporting Figures 1, 2, 3, and 4. This material is available free of charge via the Internet at http://pubs.acs.org.

MP9002317

Macromolecular Journals

Macromolecular
Rapid Communications

Enhanced in vivo Magnetic Resonance Imaging of Tumors by PEGylated Iron-Oxide–Gold Core–Shell Nanoparticles with Prolonged Blood Circulation Properties[a]

Michiaki Kumagai,[†] Tridib Kumar Sarma,[†] Horacio Cabral, Sachiko Kaida, Masaki Sekino, Nicholas Herlambang, Kensuke Osada, Mitsunobu R. Kano, Nobuhiro Nishiyama, Kazunori Kataoka*

High-density poly(ethylene glycol) (PEG)-coated iron-oxide–gold core–shell nanoparticles (AuIONs) were developed as T_2-weighted magnetic resonance imaging (MRI) contrast agents for cancer imaging. The PEG-coated iron-oxide–gold core–shell nanoparticles (PEG-AuIONs) were approximately 25 nm in diameter with a narrow distribution. Biodistribution experiments in mice bearing a subcutaneous colon cancer model prepared with C26 murine colon adenocarcinoma cells showed high accumulation of the PEG-AuIONs within the tumor mass and low nonspecific accumulation in the liver and spleen, resulting in high specificity to solid tumors. T_2-weighted MR images following intravenous injection of PEG-AuIONs showed selective negative enhancement of tumor tissue in an orthotopic pancreatic cancer model prepared with Mia-PaCa-2 human pancreatic adenocarcinoma cells. These results indicate that PEG-AuIONs are a promising MRI contrast agent for diagnosis of malignant tumors, including pancreatic cancer.

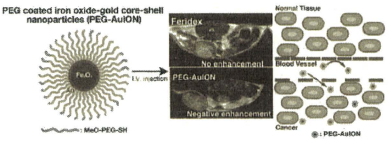

K. Kataoka, M. Kumagai, H. Cabral, S. Kaida, N. Nishiyama
Division of Clinical Biotechnology, Center for Disease Biology and Integrative Medicine, Graduate School of Medicine, The University of Tokyo, Tokyo 113-0033, Japan
Fax: +81-3-5841-7139, E-mail: kataoka@bmw.t.u-tokyo.ac.jp
K. Kataoka, T. K. Sarma, K. Osada
Department of Materials Engineering, Graduate School of Engineering, The University of Tokyo, 7-3-1 Hongo, Bunkyo-ku, Tokyo 113-8656, Japan

M. Sekino
Department of Advanced Energy, Graduate School of Frontier Science, The University of Tokyo, 5-1-5, Kashiwanoha, Kashiwa, Chiba 277-8561, Japan
N. Herlambang
Department of Mechano-Informatics, Graduate School of Information Science and Technology, The University of Tokyo, 7-3-1 Hongo, Bunkyo-ku, Tokyo 113-8656, Japan
M. R. Kano
Department of Molecular Pathology, Graduate School of Medicine, The University of Tokyo, 7-3-1 Hongo, Bunkyo-ku, Tokyo 113-0033

[a] Supporting information for this article is available at the journal's homepage at http://www.mrc-journal.de, or from the author.

[†] These authors contributed equally to the work.

© 2010 WILEY-VCH Verlag GmbH & Co. KGaA, Weinheim

DOI: 10.1002/marc.201000341

Introduction

Pancreatic cancer is a highly aggressive cancer characterized by high invasiveness and acute resistance to chemo- and radiotherapy; consequently, it represents one of the most difficult malignancies to detect and treat.[1–2] Patient prognosis is often dismal due to late diagnosis and a lack of effective therapies. This outlook could be improved by realization of diagnostic tools useful at earlier stages of the disease.

Magnetic resonance imaging (MRI) is a powerful and noninvasive technique for medical imaging of soft tissues. MRI offers clinical feasibility for molecular imaging because it provides superb anatomic resolution and contrast for visualizing tissue morphology and anatomical details of organs in vivo.[3–6] Development of contrast agents has been central to advances in MRI techniques for early diagnosis of cancer and detection of biological processes at the cellular and molecular level. Particularly, superparamagnetic iron oxide nanoparticles are gaining popularity for MRI applications in vivo, due to their low toxicity and excellent magnetic susceptibility. These superparamagnetic iron oxide nanoparticles are extremely effective for promoting proton relaxation with significant capacity to reduce MRI signal, and this effect is further enhanced by using spin echo sequences with a longer echo time (T_2-weighted imaging).[7] Thus, the accumulation site of iron oxide nanoparticles exhibits negative enhancement of MRI signals in T_2-weighted MR images. In order to enhance the in vivo utility to include use for tumor diagnosis, iron oxide nanoparticles should be highly biocompatible, of appropriate size, and should have sufficiently long blood circulation time to allow for passive tumor accumulation through the enhanced permeability and retention (EPR) effect.[8–10] Surface modification of iron oxide nanoparticles with biocompatible polymers can avoid or effectively reduce recognition by the reticuloendothelial system (RES), thus improving their circulating properties.

Poly(ethylene glycol) (PEG) has found widespread clinical use as a biocompatible, nonspecific protein resistant material that prolongs the circulation time of protein therapeutics.[11–12] PEG-based block copolymers and PEGylated liposomes have been used to improve the stability and pharmacokinetics of iron oxide nanoparticles in the physiological environment.[13–14] Many groups showed negative enhancement at the hypervascular tumor site in tumor-bearing mice using PEG-coated iron oxide nanoparticles and T_2-weighted MR imaging.[15–16] We also reported PEG-coated iron oxide nanoparticles with a hydrodynamic diameter of ≈100 nm as a negative contrast agent for successful MR imaging of subcutaneous colon tumor models.[17] However, there are no reports to enhance the MR imaging of pancreatic tumors using PEG-coated iron oxide nanoparticles without targetable biomolecules, because PEG-coated iron oxide nanoparticles developed to date have limited circulation in the blood compartment and are too large to penetrate into pancreatic tumors. In fact, without intraperitoneal administration of transforming growth factor-β (TGF-β) inhibitor, PEG-coated iron oxide nanoparticles (≈100 nm) failed to accumulate into a subcutaneous BxPC3 pancreatic tumor model, which is characterized by hypovascularity and thick fibrosis.[18] We have recently found that the size upper limit of the nanoparticle system for passive targeting to pancreatic tumor models is ≈50 nm (unpublished data). Hence, we hypothesized that with proper control of the size and surface properties of iron oxide based nanoparticles, development of effective T_2-weighted MRI contrast agents for in vivo detection of pancreatic tumors could be possible.

Recently, gold-coated superparamagnetic core–shell nanoparticles have attracted considerable attention for biomedical applications.[19–23] Au and iron oxide nanoparticles are known to be biocompatible and have been used extensively for optical- and magnetic-based applications, respectively.[24–25] Furthermore, a gold coating on the magnetic nanoparticles is stable under biological conditions and can be further functionalized with sulfur-containing moieties through Au–S bonding.

In this report, we developed PEG-coated iron-oxide–gold core–shell nanoparticles (PEG-AuIONs) for use as a T_2-weighted MRI contrast agent for imaging of pancreatic tumor models. In our method, the overall size of the nanoparticle was controlled by coating iron oxide nanoparticles with Au that allowed for reaction with methoxy-PEG-thiol (MeO-PEG-SH) and subsequent formation of a high-density PEG coating on the surface through Au–S bonding, without the formation of any higher-order assemblies. Our results demonstrated that PEG-AuIONs showed prolonged blood circulation and enhanced MR imaging of subcutaneous colon and orthotopic pancreatic tumor models. These findings suggest that our method, which allows precise control of hydrodynamic size and effective PEG density on the iron-oxide–gold core–shell nanoparticle (AuION), could be a promising method for development of MRI contrast agents for various tumor types including pancreatic cancer.

Experimental Part

AuION was synthesized with a slight modification of a previously reported method.[20,26] Hydrogen tetrachloroaurate was reduced by oleylamine to form a thin gold layer onto oleylamine and oleic acid stabilized iron oxide nanoparticles. MeO-PEG-SH ($\overline{M}_w$: 2 000) was introduced onto the surface of AuIONs through a sequential coating process in chloroform and then in methanol, followed by a solvent exchange to water. Details of PEG-AuION synthesis and characterization are provided in the Supporting Information (SI). The biodistribution of PEG-AuIONs, including tumor accumulation, was evaluated in tumor-bearing mice by measuring the Au content in blood and tissues using inductively coupled plasma–mass spectrometry (ICP-MS). In vivo MRI was performed using a 4.7 T scanner with mice bearing a subcutaneous colon (C26) or

© 2010 WILEY-VCH Verlag GmbH & Co. KGaA, Weinheim
DOI: 10.1002/marc.201000341

orthotopic pancreatic (MiaPaCa) tumor. All the details regarding physicochemical and biological studies are provided as SI.

Results and Discussion

Synthesis of PEG-Coated Iron-Oxide–Gold Core–Shell Nanoparticles (AuION)

Figure 1a shows the schematic representation for preparation of the PEG-AuIONs used in this study. First, nearly monodispersed γ-Fe_2O_3 nanoparticles with an average diameter of 10.5 ± 1.6 nm were obtained by thermal decomposition of $Fe(CO)_5$ in the presence of the capping agents oleylamine and oleic acid (5:1), under aerobic conditions with a slight modification of a previously reported method.[26] A small amount of oleic acid was added into the reaction mixture to avoid the formation of γ-Fe_2O_3 nanoparticles with different shapes. In the next step, Au was coated onto the γ-Fe_2O_3 nanoparticle surface by the reduction of $HAuCl_4$ with oleylamine at 140 °C in

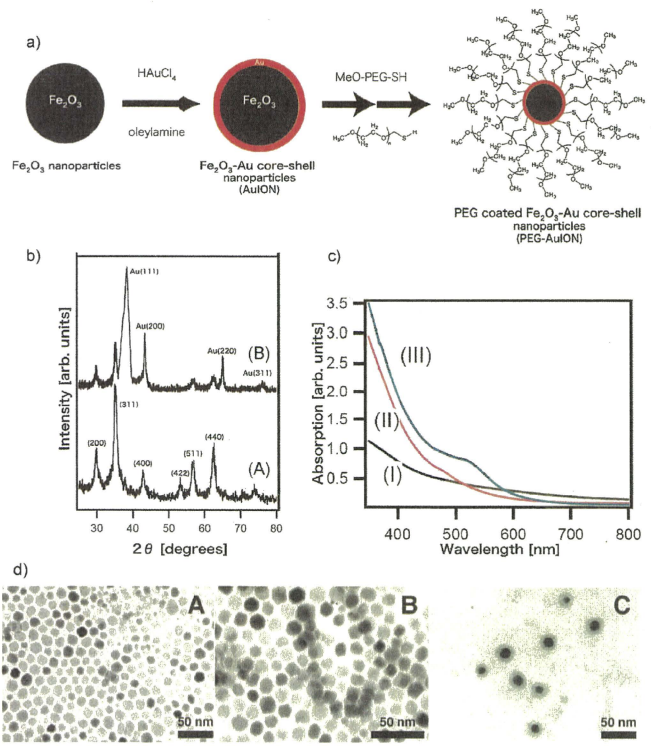

Figure 1. Preparation and properties of PEG-AuIONs. a) Scheme for Au shell formation onto γ-Fe_2O_3 nanoparticles and subsequent coating with MeO-PEG-SH to form biocompatible PEG-AuIONs. b) X-ray diffraction pattern of γ-Fe_2O_3 nanoparticles (A) and AuIONs (B); the Braggs's reflections for both nanoparticles are shown. c) UV–visible spectra of I) γ-Fe_2O_3 nanoparticles in chloroform, II) AuIONs in chloroform, and III) PEG-AuIONs in aqueous medium. d) Transmission electron microscopy images of A) γ-Fe_2O_3 nanoparticles, B) AuIONs in chloroform, and C) PEG-AuIONs in aqueous medium. The PEG layer is visible on the AuION surface in C. The nanoparticles were stained with 1% phosphotungstic acid solution. The scale bar represents 50 nm in all TEM images.

© 2010 WILEY-VCH Verlag GmbH & Co. KGaA, Weinheim

1,2-dichlorobenzene (ODCB), where oleylamine functions as both the reducing agent and the stabilizer.[21] Oleylamine coated AuIONs were washed by several cycles of dispersion-centrifugation to remove excess oleylamine, and were finally dispersed into chloroform for further modification.

The formation of an Au shell on the γ-Fe_2O_3 nanoparticles was confirmed by X-ray diffraction measurement as shown in Figure 1b. Evolution of Bragg's diffraction peaks from the face-centered cubic (fcc) lattice structure of Au are clearly visible from the X-ray diffraction spectra of AuIONs. Using the Debye–Scherer equation, the thickness of Au on the γ-Fe_2O_3 surface was calculated to be 1.3 nm. Transmission electron microscopy (TEM) studies (Figure 1d(A,B)) showed that the average particle size increased by 1.5 ± 0.6 nm following Au deposition onto the γ-Fe_2O_3 nanoparticles, which is comparable to the thickness of Au calculated from the X-ray diffraction peaks.

PEG was readily conjugated to the particle surface by reaction of PEG-SH with the gold surface through well-known thiol–gold coupling chemistry. After a single cycle of PEG modification, followed by the evaporation of chloroform under vacuum, PEG-AuIONs were readily soluble in aqueous medium. However, when the nanoparticles were incubated for 12 h in 150×10^{-3} M NaCl solution, agglomeration occurred, suggesting incomplete coating of MeO-PEG-SH on the nanoparticle surface (data not shown). Therefore, repetitive PEG coating onto PEG-AuIONs (described in SI) was performed to increase the PEG density on the particle surface, as it has been reported that the process involving repetitive PEG adsorption significantly contributes to increase the PEG density on the gold surface.[27] Salt-induced agglomeration of PEG-AuIONs obtained by this double PEG coating process was avoided, even after transfer into aqueous media through dialysis, suggesting the formation of a PEG layer with appreciably high density around the AuION surface. PEG-AuIONs stored in 10×10^{-3} M Tris-HCl buffer containing 0.03% bovine serum albumin were stable for several months without any notable aggregation. Use of methanol as the solvent for the second cycle of PEG coating also proved to be crucial for controlling particle size and dispersity of the PEGylated nanoparticles, as application of the second PEG coating onto the AuIONs in water resulted in low quality particles with large hydrodynamic diameter and high polydispersity index (data not shown).

The formation of an Au shell on the γ-Fe_2O_3 surface was further confirmed by UV–vis spectroscopy of the PEG-AuION in aqueous medium. As shown in Figure 1c, AuIONs did not show any characteristic plasmon resonance in organic medium as AuIONs are protected by the long chain alkyl ligands. However, when the AuION was transferred to the aqueous medium as a PEGylated nanoparticle, a plasmon resonance band appears with absorption at 515 nm, probably due to the increased dielectric constant of the medium.

Characterization of PEG-Coated Iron-Oxide–Gold Core–Shell Nanoparticles (PEG-AuION)

The TEM image of PEG-AuION transferred to water after surface modification with MeO-PEG-SH (Figure 1d(C)) showed no apparent agglomeration. Furthermore, the PEG layer surrounding the AuION core was visible in TEM after negative staining with 1% phosphotungstic acid as seen in Figure 1d(C). The thickness of the PEG layer was determined to be 6.5 ± 1.2 nm from this TEM image.

The neutral ζ-potential of 0.49 ± 0.12 mV of PEG-AuIONs in water showed complete passivation of the nanoparticle surface with the PEG layer. The number of PEG molecules (molecular weight = 2 kDa) on the surface of a single 12.9 nm AuION was calculated to be ~2500 by thermogravimetric analysis (TGA) analysis of the sample under N_2 atmosphere. This surface coverage corresponds to a footprint area of 0.25 nm^2 per PEG molecule, which is significantly smaller than previous reports for MeO-PEG-SH conjugated on Au nanoparticle surfaces (2.42 nm^2).[28–29] This result suggests that the PEG-AuION possesses an appreciably dense PEG layer. Chain conformation of grafted PEG on a surface plane is estimated to be an extended brush at this density (0.25 nm^2). Nevertheless, on a spherical surface, PEG density decreases in a radial direction toward the exterior of the particle with a change in the PEG conformation from brush to random coil (a mushroom model).[30] Note that the height of PEG 2 kDa in a mushroom conformation is estimated to be 3.3 nm (twice of radius of gyration (R_g)) as lower limit,[31] whereas the height in an extended conformation is estimated to be 15.9 nm as upper limit by using the effective monomer length of PEG in water ($2000/44 \times 0.35 = 15.9$ nm).[32] The PEG thickness estimated from the TEM image for PEG-AuIONs obtained in this study (6.5 ± 1.2 nm) is in the range between these lower and upper estimated heights of PEG in the extended brush and random coil conformation.

The dispersion stability of PEG-AuIONs against increased NaCl concentration in aqueous solution was evaluated by dynamic light scattering (DLS) measurement, which revealed that the hydrodynamic diameter remained constant up to 1 M NaCl (Figure 2a). Furthermore, there was no change in the diameter of PEG-AuIONs even after 12 h incubation in 10×10^{-3} M Tris-HCl buffer containing 10% fetal bovine serum at pH 7.4 and 37 °C (Figure 2b). PEG-AuIONs were also found to be stable in buffer within the pH range of 3–10.

To examine the feasibility of PEG-AuIONs as a T_2–weighted MRI contrast agent, we evaluated the relaxivity r_2 of PEG-AuIONs and determined the value to be $149.32 \times 10^{-3}\ M^{-1} \cdot s^{-1}$ (Figure 2c). This r_2 value is comparable to the commercially

© 2010 WILEY-VCH Verlag GmbH & Co. KGaA, Weinheim
DOI: 10.1002/marc.201000341

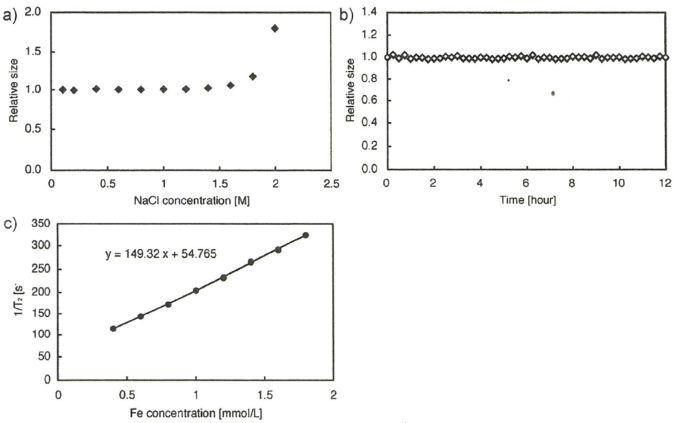

Figure 2. a) Change in the relative particle size of PEG-AuIONs with increased NaCl concentration, determined by DLS measurement. b) Time-dependency of the relative size of PEG-AuIONs in Tris-HCl buffer containing 10% fetal bovine serum at 37 °C. c) Relaxivity r_2 of PEG-AuIONs using the Carr-Purcell-Meiboom-Gill (CPMG) pulse sequence at 25 °C, 0.59 T.

available T_2 contrast agent Feridex (dextran-coated iron oxide nanoparticles).

Biodistribution of PEGylated Fe2O3-Au Core–Shell Nanoparticles

Figure 3 shows the concentration of gold in blood plasma over time after intravenous administration of PEG-AuIONs. The gold concentration measured in plasma indicates that PEG-AuIONs stably circulate in the blood compartment with 8% of the injected dose observed even after 24 h. Prolonged blood circulation of the PEG-AuION was reasonably associated with high stability of PEG-AuIONs under physiological conditions at 37 °C (Figure 2). Accumulation of PEG-AuIONs within solid tumor and normal tissues (liver, kidney, spleen and muscle) is also shown in Figure 3. Notably, PEG-AuION showed continuous accumulation with time into solid tumors, while its accumulation to other tissues was somewhat limited.

To assess the selectivity towards the solid tumors, the area under the Au concentration–time curve (AUC) and AUC ratios of the tumor to normal tissues at 24 h after injection were determined and are shown in Supplementary Table 1 in the SI. PEG-AuIONs exhibited ratios $AUC_{tumor}/AUC_{organ} > 1.0$ for spleen, kidney, and muscle tissues, indicating selectivity to the tumor (AUC_{tumor}/AUC_{organ} of 2.84, 1.21, and 67.27 for spleen, kidney, and muscle tissues, respectively). These AUC_{tumor}/AUC_{organ} ratios are comparable to those observed for so-called stealth drug carriers.[33] However, AUC_{tumor}/AUC_{liver} ratio is somewhat low at 0.95. This may be due to the relatively high blood volume in the liver. Note that liver has about one-fifth of blood volume in the body, and the liver accumulation value for PEG-AuIONs has a substantial contribution from PEG-AuIONs present in the blood pool.

In vivo Tumor Imaging

In order to study the efficacy of PEG-AuIONs for dynamic in vivo MRI, imaging of tumor tissue was conducted and compared with the commercially available MRI contrast agent Feridex (dextran-coated iron oxide nanoparticles). First, we performed in vivo MRI with nude mice bearing subcutaneously inoculated murine colon adenocarcinoma (C26) cells (Figure 4a,b). Negative enhancement of the tumor site in T_2-weighted images, which is indicated as circled by red line in Figure 4, gradually increased 5 min after injection of PEG-AuIONs, with a maximum negative enhancement of 60% observed at 4 h post-injection (Figure 4a,e and Table 1). Note that MRI signals in other organs and tissues surrounding the tumor were also negatively enhanced in T_2-weighted images due to the existence of high concentration of PEG-AuIONs in the blood circulation. Therefore, the percentile rates of negative enhancement at 4 h post-injection of PEG-AuIONs were compared between in the tumor and the intestine

© 2010 WILEY-VCH Verlag GmbH & Co. KGaA, Weinheim

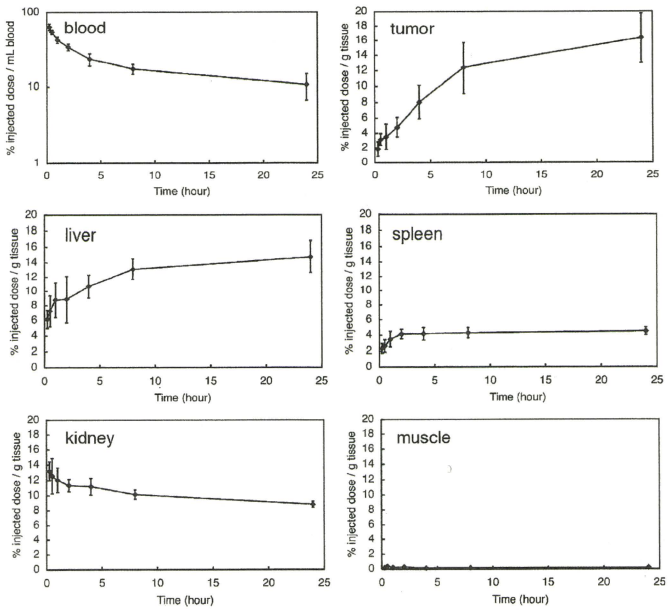

Figure 3. Biodistribution of PEG-AuIONs. The levels of Au in blood, tumor, liver, spleen, kidney, and muscles are shown as percentage of dose at each time after intravenous injection.

(indicated as circled by yellow line in MR images) (Table 1), suggesting that PEG-AuIONs reduced MRI signals more efficiently in the tumor compared with intestine. In contrast, Feridex failed to reduce MRI signals selectively in the tumor even after 4 h (Figure 4b,e and Table 1), presumably due to non-specific accumulation in the RES.

Next, we tested the efficacy of the PEG-AuIONs in an orthotopic pancreatic cancer model, using MiaPaCa-2 cells derived from human pancreatic cancer. The T_2-weighted MR images of the tumor region over time are shown in Figure 4c,d. Noticeable negative enhancement (~25%) was observed as soon as 5 min after administration of PEG-AuIONs, and continued even 4 h after administration (Figure 4c,f and Table 2). It should be noted that PEG-AuIONs exhibited focal MRI signal enhancement in the tumor tissue (indicated by red arrowhead in Figure 4c), presumably due to their heterogeneous intratumoral distribution. The rate of negative enhancement in those regions was calculated to be 47%, which was appreciably higher than that in the intestine (18%) (Table 2). In contrast, Feridex failed in the tumor-selective MRI signal enhancement in this model (Figure 4d,f and Table 2). Furthermore, we tested the effects of the PEG-AuION system compared to Feridex in a model representing metastatic foci in the liver using MiaPaCa-2 cells (Supplementary Figure 1a,b and Supplementary Table 2 in the SI), and the results were consistent with those obtained in the orthotopic model described above. The accumulation of PEG-AuIONs in

Table 1. Percentile rate of negative enhancement in MR signals in the tumor and intestine at 4 h post-injection of PEG-AuION and Feridex into mice bearing a subcutaneous model of murine colon adenocarcinoma (C26) celles.

	Negative enhancement in MRI signals	
	Tumor	Intestine
PEG-AuION	60%	25%
Feridex	5%	8%

© 2010 WILEY-VCH Verlag GmbH & Co. KGaA, Weinheim
DOI: 10.1002/marc.201000341

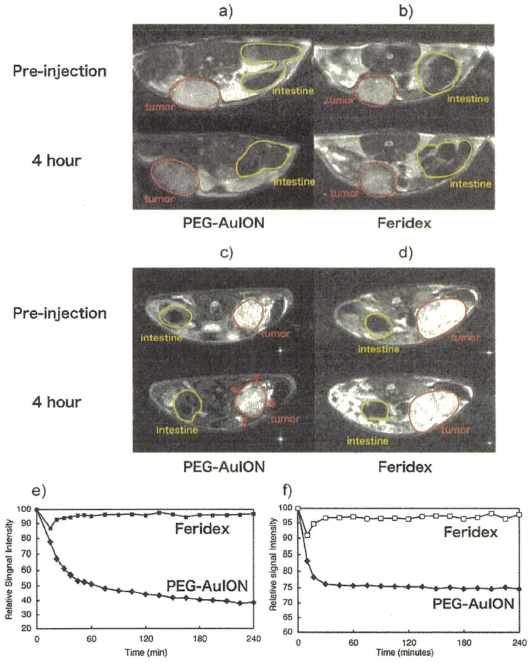

Figure 4. In vivo MR imaging of tumors. a,b) T_2-weighted images of subcutaneous C26 murine carcinoma (tumor sites are circled by red line) at 4 h after intravenous injection of PEG-AuIONs (a) and Feridex (b). c,d) T_2-weighted images of an orthotopic MiaPaCa-2 human pancreatic cancer model (tumor sites are circled by red line) at 4 h after intravenous injection of PEG-AuIONs (c) and Feridex (d). All images were obtained in a magnetic field strength of 4.7 T. Time-dependencies of relative signal intensities at the tumor site in T_2-weighted images after injection of PEG-AuIONs and Feridex in C26 subcutaneous tumor model (e) and in MiaPaCa-2 orthotopic tumor model (f).

metastatic foci was confirmed histologically using silver staining against gold particles (Supplementary Figure 1c in the SI). These results suggest successful MR imaging of malignant tumors is feasible using PEG-AuIONs.

Conclusion

In this study, we have demonstrated that AuIONs of sub-50-nm size and coated with a dense PEG brush can be used as an MRI contrast agent for a variety of tumors, including pancreatic tumors. The relatively small hydrodynamic diameter along with a high PEG density facilitated extended circulation of PEG-AuIONs, which allowed for accumulation into pancreatic cancer models through the EPR effect. These results imply that with proper control of the structural and surface properties of the nanoparticles, it is feasible to develop effective MRI contrast agents for the diagnosis of intractable tumors such as pancreatic cancer, even without attachment of cell-targeting ligands. The presence of an Au shell on the magnetic nanoparticle not only offers the possibility for surface modification with various biomolecules for biomarker-targeted imaging, but also offers another detection modality through various techniques such as X-ray tomography[34–35] (CT) and surface-enhanced Raman scattering (SERS).[36] The ultimate goal of nanoparticle materials for medical research is to develop high-performance systems for both detection and treatment of biological events such as cancer metastasis and real-time visualization of biological events at the cellular and molecular level,

Table 2. Percentile rate of negative enhancement in MR signals in the tumor and intestine at 4 h post-injection of PEG-AuION and Feridex into mice bearing an orthotopic model of human pancreatic adenocarcinoma (MiaPaCa-2) cells.

	Negative enhancement in MRI signals		
	Tumor (whole)	Tumor (arrow head[a])	Intestine
PEG-AuION	25%	47%	18%
Feridex	3%	–	6%

[a]The rate of negative enhancement of MRI signals in the regions indicated by red arrowhead in Figure 4c was calculated.

© 2010 WILEY-VCH Verlag GmbH & Co. KGaA, Weinheim

leading to better prognosis in patients bearing tumor. The results of this study represent a significant improvement in nanoparticle-based tumor detection, which may prove useful for clinical applications and also in the design of more advanced systems.

Acknowledgements: The authors thank Dr. *James R. Christie II*, The University of Tokyo, for editing the English of the manuscript. This research was supported by the *Japan Society for the Promotion of Science (JSPS)* through its "Funding Program for World-Leading Innovative R&D on Science and Technology (FIRST Program)". We are grateful to Dr. *S. Fukuda*, The University of Tokyo Hospital, for his valuable support in the TEM measurement. T. K. S. acknowledges a fellowship from the *Japan Society for the Promotion of Science (JSPS)*.

Received: June 8, 2010; Revised: June 30, 2010; DOI: 10.1002/marc.201000341

Keywords: gold coatings; iron oxide; magnetic resonance imaging; nanoparticles; poly(ethylene glycol)

[1] A. Jemal, R. Siegel, E. Ward, Y. P. Hao, J. Q. Xu, M. J. Thun, *CA-A Cancer Journal For Clinicians* **2009**, *59*, 225.
[2] M. J. MacKenzie, *Lancet Oncology* **2004**, *5*, 541.
[3] R. Weissleder, A. Moore, U. Mahmood, R. Bhorade, H. Benveniste, E. A. Chiocca, J. P. Basilion, *Nat. Med.* **2000**, *6*, 351.
[4] H. B. Na, I. C. Song, T. Hyeon, *Adv. Mater.* **2009**, *21*, 1.
[5] Y. W. Jun, J. H. Lee, J. Cheon, *Angew. Chem., Int. Ed.* **2008**, *47*, 5122.
[6] S. Laurent, D. Forge, M. Port, A. Roch, C. Robic, L. V. Elst, R. N. Muller, *Chem. Rev.* **2008**, *108*, 2064.
[7] Y. J. Wang, S. M. Hussain, G. P. Krestin, *Eur. Radiol.* **2001**, *11*, 2319.
[8] Y. Matsumura, H. Maeda, *Cancer Res.* **1986**, *46*, 6387.
[9] H. Maeda, J. Fang, T. Inutsuka, Y. Kitamoto, *Int. Immunopharmacol.* **2003**, *3*, 319.
[10] D. M. McDonald, P. Baluk, *Cancer Res.* **2002**, *62*, 5381.
[11] J. M. Harris, R. B. Chess, *Nat. Rev Drug Discov.* **2003**, *2*, 214.
[12] K. Kataoka, A. Harada, Y. Nagasaki, *Adv. Drug. Delivery Rev.* **2001**, *47*, 113.
[13] C. Khemtong, C. W. Kessinger, J. M. Ren, E. A. Bey, S. G. Yang, J. S. Guthi, D. A. Boothman, A. D. Sherry, J. M. Gao, *Cancer Res.* **2009**, *69*, 1651.
[14] J. F. Berret, N. F. Schonbeck, F. Gazeau, D. El Kharrat, O. Sandre, A. Vacher, M. Airiau, *J. Am. Chem. Soc.* **2006**, *128*, 1755.
[15] H. Lee, M. K. Yu, S. Park, S. Moon, J. J. Min, Y. Y. Jeong, H.-W. Kang, S. Jon, *J. Am. Chem. Soc.* **2007**, *129*, 12739.
[16] E. K. U. Larsen, T. Nielsen, T. Wittenborn, H. Birkedal, T. Vorup-Jensen, M. H. Jakobsen, L. Østergaard, M. R. Horsman, F. Besenbacher, K. A. Howard, J. Kjems, *ACS Nano*, **2009**, *3*, 1947.
[17] M. Kumagai, Y. Imai, M. T. Nakamura, Y. Yamasaki, M. Sekino, S. Ueno, K. Hanaoka, K. Kikuchi, T. Nagano, E. Kaneko, K. Shimokado, K. Kataoka, *Colloids Surf. B* **2007**, *56*, 174.
[18] M. Kumagai, M. R. Kano, Y. Morishita, M. Ota, Y. Imai, N. Nishiyama, M. Sekino, S. Ueno, K. Miyazono, K. Kazunori, *J. Control. Release* **2009**, *140*, 306.
[19] J. L. Lyon, D. A. Fleming, M. B. Stone, P. Schiffer, M. E. Williams, *Nano Lett.* **2004**, *4*, 719.
[20] L. Y. Wang, J. Luo, Q. Fan, M. Suzuki, I. S. Suzuki, M. H. Engelhard, Y. H. Lin, N. Kim, J. Q. Wang, C. J. Zhong, *J. Phys. Chem. B* **2005**, *109*, 21593.
[21] Z. Xu, Y. Hou, S. Sun, *J. Am. Chem. Soc.* **2007**, *129*, 8698.
[22] D. Kim, J. W. Kim, Y. Y. Jeong, S. Jon, *Bull. Korean Chem. Soc.* **2009**, *30*, 1855.
[23] H. Kojima, Y. Mukai, M. Yoshikawa, K. Kamei, T. Yoshikawa, M. Morita, T. Inubushi, T. A. Yamamoto, Y. Yoshioka, N. Okada, S. Seino, S. Nakagawa, *Bioconjugate Chem.* **2010**, *21*, 1026.
[24] S.-J. Cho, B. R. Jarrett, A. Y. Louie, S. M. Kauzlarich, *Nanotechnology* **2006**, *17*, 640.
[25] T. A. Larson, J. Bankson, J. Aaron, K. Sokolov, *Nanotechnology* **2007**, *18*, 325101.
[26] J. W. Cheon, N. J. Kang, S. M. Lee, J. H. Lee, J. H. Yoon, S. J. Oh, *J. Am. Chem. Soc.* **2004**, *126*, 1950.
[27] K. Uchida, H. Otsuka, M. Kaneko, K. Kataoka, Y. Nagasaki, *Anal. Chem.* **2005**, *77*, 1075.
[28] S. Takae, Y. Akiyama, H. Otsuka, T. Nakamura, Y. Nagasaki, K. Kataoka, *Biomacromolecules* **2005**, *6*, 818.
[29] W. P. Wuelfing, S. M. Gross, D. T. Miles, R. W. Murray, *J. Am. Chem. Soc.* **1998**, *120*, 12696.
[30] K. Ohno, T. Morinaga, S. Takeno, Y. Tsujii, T. Fukuda, *Macromolecules* **2007**, *40*, 9143.
[31] S. Kawaguchi, G. Imai, J. Suzuki, A. Miyahara, T. Kitano, K. Ito, *Polymer* **1997**, *38*, 2885.
[32] A. K. Kenworthy, K. Hristova, D. Needham, T. J. McIntosh, *Biophys. J.* **1995**, *68*, 1921.
[33] H. Cabral, N. Nishiyama, K. Kataoka, *J. Controlled Release* **2007**, *121*, 146.
[34] Q. Y. Cai, S. H. Kim, K. S. Choi, S. Y. Kim, S. J. Byun, K. W. Kim, S. H. Park, S. K. Juhng, K. H. Yoon, *Investigative Radiology* **2007**, *42*, 797.
[35] D. Kim, S. Park, J. H. Lee, Y. Y. Jeong, S. Jon, *J. Am. Chem. Soc.* **2007**, *129*, 7661.
[36] X. Qian, X. H. Peng, D. O. Ansari, Q. Yin-Goen, G. Z. Chen, D. M. Shin, L. Yang, A. N. Young, M. D. Wang, S. M. Nie, *Nat. Biotechnol.* **2008**, *26*, 83.

© 2010 WILEY-VCH Verlag GmbH & Co. KGaA, Weinheim

Cancer Research

Visible Drug Delivery by Supramolecular Nanocarriers Directing to Single-Platformed Diagnosis and Therapy of Pancreatic Tumor Model

Sachiko Kaida[1,3,7], Horacio Cabral[1,3], Michiaki Kumagai[1], Akihiro Kishimura[2], Yasuko Terada[4], Masaki Sekino[5], Ichio Aoki[6], Nobuhiro Nishiyama[1,3], Toru Tani[7], and Kazunori Kataoka[1,2,3]

Abstract

Nanoparticle therapeutics are promising platforms for cancer therapy. However, it remains a formidable challenge to assess their distribution and clinical efficacy for therapeutic applications. Here, by using multifunctional polymeric micellar nanocarriers incorporating clinically approved gadolinium (Gd)–based magnetic resonance imaging contrast agents and platinum (Pt) anticancer drugs through reversible metal chelation of Pt, simultaneous imaging and therapy of an orthotopic animal model of intractable human pancreatic tumor was successfully performed without any serious toxicity. The strong tumor contrast enhancement achieved by the micelles correlated with the 24 times increase of r_1 of the Gd chelates, the highest for the formulations using clinically approved Gd chelates reported to date. From the microsynchrotron radiation X-ray fluorescence spectrometry scanning of the lesions, we confirmed that both the Gd chelates and Pt drugs delivered by the micelles selectively colocalized in the tumor interior. Our study provides new insights for the design of theranostic micelles with high contrast enhancement and site-specific clinical potential. *Cancer Res; 70(18); 7031–41. ©2010 AACR.*

Introduction

Recently, there has been explosive development of chemotherapeutic agents for cancer, but the efficacies of anticancer drugs are still insufficient particularly for the treatment of intractable tumors, including pancreatic cancer. Although the latest advances in molecular targeting agents have shown specific efficiency, the survival time of patients is often extended only slightly, even when these agents are used in combination with other anticancer drugs. Moreover, the use of such drugs typically results in various characteristic side effects, such as interstitial pneumonia for gefitinib (1), cardiotoxicity for trastuzumab (2, 3), and thrombosis for bevacizumab (4). Alternatives to developing these compounds and antibodies selective for cancer cells, with the aim of modulating drug distribution in the body to accomplish selective drug accumulation in the tumor site, are thus needed, and for this purpose, nanometric-scale vehicles or nanocarriers directing therapeutics to the tumor site are a key platform.

In the last decade, several kinds of nanoparticle therapeutics platforms, including liposomes, nanoparticles, and polymeric micelles, have been developed to selectively deliver drugs to tumor sites (5–12). These approaches have been used to improve the therapeutic efficacy and to reduce the side effects of drugs incorporated in delivery carriers (13, 14), and nanoparticle therapeutics such as Doxil (15) or Abraxane (16) are already in clinical use. The tumor targeting of these nanoparticle therapeutics is based on the enhanced permeability and retention (EPR) effect (in other words, the increased accumulation of high–molecular weight compounds, such as nanoparticles, in tumor tissue due to the high permeability of tumor blood vessels and the retention of these compounds because of the impaired lymphatic drainage at the cancer site; ref. 17). In the late 1980s, we developed one of the auspicious nanoparticle therapeutics, polymeric micelles, a self-assembly of amphiphilic block copolymers consisting of hydrophobic segments forming the drug-loaded core and water-soluble segments forming the biocompatible shell (11, 12). The main advantages of this system are the possibility of incorporating a variety of drugs, including hydrophobic substances, metal complexes, and charged macromolecules such as nucleic acids, as well as controlling their release properties by engineering and modifying the micelle-forming block copolymers. Moreover, polymeric micelles can be designed to be responsive to environmental changes and capable of target

Authors' Affiliations: [1]Center for Disease Biology and Integrative Medicine, Graduate School of Medicine, [2]Department of Materials Engineering, Graduate School of Engineering, and [3]Center for NanoBio Integration, The University of Tokyo, Tokyo, Japan; [4]Japan Synchrotron Radiation Research Institute, SPring-8, Hyogo, Japan; [5]Department of Advanced Energy, Graduate School of Frontier Sciences, The University of Tokyo, Chiba, Japan; [6]Molecular Imaging Center, National Institute of Radiological Sciences, Chiba, Japan; and [7]Department of Surgery, Shiga University of Medical Science, Shiga, Japan

Note: Supplementary data for this article are available at Cancer Research Online (http://cancerres.aacrjournals.org/).

Corresponding Author: Kazunori Kataoka, Department of Materials Engineering, Graduate School of Engineering, The University of Tokyo, 7-3-1 Hongo, Bunkyo-ku, Tokyo 113-8656, Japan. Phone: 81-3-5841-7138; Fax: 81-3-5841-7139; E-mail: kataoka@bmw.t.u-tokyo.ac.jp.

doi: 10.1158/0008-5472.CAN-10-0303

©2010 American Association for Cancer Research.

recognition. Our micelle formulations incorporating Adriamycin, paclitaxel, SN-38, cisplatin, and DACHPt (activated oxaliplatin; NK911, NK105, NK012, NC6004, and NC4016, respectively) are being examined in clinical studies, and four of these formulations have advanced to phase II studies (18–21). These clinical studies have revealed that polymeric micelles showed reduced side effects and high effectiveness against various intractable tumors, including triple-negative breast cancers that do not express the genes for estrogen receptor, progesterone receptor, and Her2/neu (22). Consequently, polymeric micelles have been considered one of the most promising drug delivery systems (DDS) in the field of cancer chemotherapy.

Although a crucial breakthrough in cancer treatment has been achieved using several micelles, the methods for estimating the distribution and effectiveness of the micelles are ineffective and inadequate. The precise monitoring of their distribution and early feedback on treatment efficacy would allow clinicians to anticipate the therapeutic process in each cancer patient and customize medicine for cancer therapy. Thus, it is imperative to directly assess the biodistribution of the micelles and their cargo as well as the magnitude of their accumulation at the cancer site. Consequently, the development of micelles with both imaging and therapeutic functions [theranostic (23) micelles] will permit visualization of the distribution of the micelles inside the body and tumor in a real-time manner, allowing optimization of the treatment protocol according to the unique characteristics of the malignancies in individual patients (24–26).

We developed theranostic core-shell polymeric micelles based on the self-assembly of block copolymers with both a magnetic resonance imaging (MRI) function and cancer therapeutic capacity. The micelles incorporate gadolinium–diethylenetriaminepentaacetic acid (Gd-DTPA), a widely used T_1-weighted MRI (T1W) contrast agent (27), and (1,2-diaminocyclohexane)platinum(II) (DACHPt), the parent complex of the potent anticancer drug oxaliplatin, in their core by reversible complexation between DACHPt, Gd-DTPA, and poly(ethylene glycol)-*b*-poly(glutamic acid) [PEG-*b*-P(Glu); Fig. 1]. Accordingly, both the DACHPt and Gd-DTPA complexes, which can be excreted from the kidney, thus avoiding toxicity from long-term accumulation inside the body, are released from the micelles in a sustained manner under physiologic conditions. Moreover, the longitudinal relaxivity (r_1) of the micelles (i.e., their ability as an MRI contrast agent) increased ~24 times compared with that of free

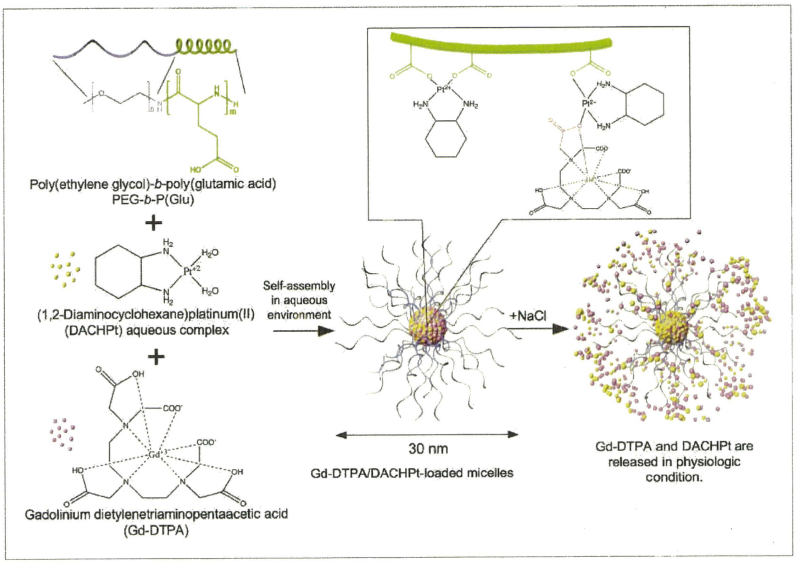

Figure 1. Schematic diagram of proposed self-assembly of Gd-DTPA/DACHPt–loaded micelles and release of Pt and Gd complexes from the micelles in chloride-containing medium.

Gd-DTPA, enabling, jointly with the enhanced tumor accumulation provided by the EPR effect, the improved detection of solid tumors. We also showed that the micelles have continuous and strong anticancer effect, and enhance the MRI contrast of the tumor region in an orthotopic human pancreatic cancer xenograft model much more intensely than Gd-DTPA alone, although the diagnosis and treatment of pancreatic cancer has been considered to be the most difficult among digestive cancers. Thus, the Gd-DTPA/DACHPt–loaded micelles are expected not only to improve the effectiveness and safety of the incorporated drugs but also to assist in the real-time monitoring of the drug distribution and tumor accumulation, suggesting the great potential of visible DDSs.

Materials and Methods

Cancer cell lines and animals

Murine colon adenocarcinoma 26 (C-26) cells were kindly supplied by the National Cancer Center. The BxPC3 human pancreatic adenocarcinoma cell line was obtained from the American Type Culture Collection. C-26 and BxPC3 cells were maintained in RPMI 1640 (Sigma-Aldrich, Inc.) containing 10% fetal bovine serum in a humidified atmosphere containing 5% CO_2 at 37°C. CDF_1 mice and BALB/c nude mice (female; 18–20 g body weight; 6 weeks old) were purchased from Charles River Japan. All animal experiments were carried out in accordance with the policies of the Animal Ethics Committee of the University of Tokyo.

Preparation of Gd-DTPA/DACHPt–loaded micelles

PEG-*b*-P(Glu) [Mw_{PEG} = 12,000 Da; polymerization degree of P(Glu) = 20] block copolymer was synthesized according to the previously described method (28). Briefly, the *N*-carboxy anhydride of γ-benzyl L-glutamate (Sigma Chemical) was synthesized by the Fuchs-Farthing method using triphosgene. Then, *N*-carboxy anhydride of γ-benzyl L-glutamate was polymerized in DMF initiated by the primary amino group of CH_3O-PEG-NH_2 (Nippon Oil and Fats) to obtain PEG-*b*-poly (γ-benzyl-L-glutamate) (PEG-*b*-PBLG). The polymerization degree was verified by comparing the proton ratios of methylene units in PEG (-OCH_2CH_2-: δ = 3.7 ppm) and phenyl groups of PBLG (-$CH_2C_6H_5$: δ = 7.3 ppm) in ^{1}H nuclear magnetic resonance (NMR) measurement (solvent: DMSO-d_6; JEOL EX270, JEOL, Inc.). PEG-*b*-PBLG was deprotected by mixing with 0.5 N NaOH at room temperature to obtain PEG-*b*-P(Glu). Complete deprotection was confirmed by ^{1}H-NMR measurement (solvent: D2O; temperature: 25°C).

Gd-DTPA (Aldrich Chemical) was converted to sodium salt by adjusting the pH to 7 with NaOH, and it was lyophilized. A 5 mmol/L solution of bis(nitrato) (*trans-l*-1,2-diaminocyclohexane)platinum(II) [DACHPt(NO_3)$_2$; W.C. Heraeus GmbH & Co. KG] in water was mixed with the sodium salt of Gd-DTPA (5 mmol/L), and the solution was maintained for 24 hours at 37°C. Then, PEG-*b*-P(Glu) ([Glu] = 5 mmol/L) was added to this solution ([DACHPt]/[Glu] = 1.0) and reacted for 120 hours at 37°C to prepare Gd-DTPA/DACHPt–loaded micelles. The micelles were purified by dialysis against distilled water [molecular weight cutoff size (MWCO): 2,000; Spectra/Por-6, Spectrum Laboratories] and by ultrafiltration (MWCO: 30,000). The size distribution of the Gd-DTPA/DACHPt–loaded micelles was evaluated by a dynamic light scattering (DLS) measurement at 25°C using a Zetasizer Nano ZS90 (Malvern Instruments). The Pt and Gd contents of the micelles were determined by inductively coupled plasma–mass spectrometry (ICP-MS; 4500 ICP-MS, Hewlett Packard).

Fourier transform IR spectra of Gd-DTPA/DACHPt aqueous complex

Fourier transform IR (FT-IR) spectra were obtained using a FT-IR spectrophotometer (FT/IR 615, JASCO Corp.) with a resolution of 4 cm^{-1}. To characterize the interaction between Gd-DTPA and DACHPt, freeze-dried Gd-DTPA/DACHPt complex at 1:1, 1:5, and 1:10 mixing ratios was milled with KBr and then pressed into a disc for analysis.

Arsenazo III colorimetric assay

The absence of Gd^{3+} in the Gd-DTPA/DACHPt mixture was confirmed by using the arsenazo III method (29). Briefly, Gd-DTPA and DACHPt were mixed at 1:1 molar ratio (0.2 mmol/L) in water. Then, 0.5 mL of this solution was mixed with 0.5 mL of arsenazo III (0.2 mmol/L; Sigma-Aldrich). The absorbance spectra were measured with a spectrometer (V-570 UV/VIS/NIR Spectrophotometer, JASCO). A calibration curve was obtained by measuring the absorbance at 660 nm of a series of standard solutions of the arsenazo III/Gd^{3+} complex prepared by mixing solutions of $GdCl_3$ (Sigma-Aldrich) and arsenazo III in water. The pH of the solutions was maintained at 6.5.

Release rate of DACHPt and Gd-DTPA from the Gd-DTPA/DACHPt–loaded micelles

The release of DACHPt and Gd-DTPA complexes from the micelles was studied by the dialysis method. One milliliter of Gd-DTPA/DACHPt–loaded micelles solution was introduced in a dialysis bag (MWCO: 6,000) and incubated in 99 mL micelles in physiologic conditions (i.e., 10 mmol/L PBS plus 150 mmol/L NaCl at 37°C). The solution outside the dialysis bag was sampled at defined periods. The concentration of Pt and Gd was measured by ICP-MS. The UV-Vis spectra of Gd-DTPA, $GdCl_3$, and the solution outside the dialysis bag were recorded from 270 nm to 280 nm with a UV-Vis spectrometer (V-570 UV/VIS/NIR Spectrophotometer).

Kinetic stability of Gd-DTPA/DACHPt–loaded micelles

The stability of the Gd-DTPA/DACHPt–loaded micelles in physiologic conditions was determined by DLS and static light scattering using a Zetasizer Nano ZS90. The changes in the light scattering intensity were measured at defined time periods. In this analysis, a decrease in the light scattering intensity was associated with a decrease in the apparent molecular weight of the micelles and drug density inside the micelle core as well as in the micelle concentration. The size distribution of the Gd-DTPA/DACHPt–loaded micelles was simultaneously monitored.

Characterization of the r_1 relaxivities

The MR contrast effect of the magnetic nanoparticles was examined by measuring their proton longitudinal relaxivities, r_1, of which the definition is the slope of the concentration dependence given as $1/T_1 = 1/T_{10} + r_1[\mathrm{Gd}]$, where T_1 is the longitudinal relaxation time, $1/T_1$ is the longitudinal relaxation rate contrast in the presence of a paramagnetic species, and $1/T_{10}$ is the longitudinal relaxation rate contrast in the absence of a paramagnetic species. The T_1 of Gd-DTPA/DACHPt–loaded micelles, Gd-DTPA, or Gd-DTPA/DACHPt solution at 0.1, 0.2, 0.3, 0.4, and 0.5 mmol/L was measured at 37°C in water with a 0.59-T ^{1}H-NMR analyzer (JNM-MU25A, JEOL) with a standard inversion-recovery pulse sequence.

Cancer models

CDF_1 mice (female, 6 weeks old) were inoculated s.c. with C-26 cells (1×10^6/mL) and used for biodistribution study, antitumor activity assay, and MRI. BALB/c nude mice (female, 6 weeks old) were inoculated in the pancreas with BxPC3 cells for biodistribution study, antitumor activity assay, and MRI. For the latter model, the mice were anesthetized by isoflurane inhalation, and the pancreas was exposed and injected subserosally with 0.1 mL of BxPC3 cells (5×10^6/mL).

Biodistribution

Biodistribution studies were carried out on C-26 tumor–bearing mice at 10 days after implantation when the mean tumor volume was ~100 mm^3. Oxaliplatin, Gd-DTPA, or Gd-DTPA/DACHPt–loaded micelles were i.v. injected to mice at a dose of 100 μg per mouse on a Pt basis or 100 μg per mouse on a Gd basis. The mice were sacrificed after defined time periods (1, 4, 8, and 24 hours). Tumors, livers, kidneys, and spleens were excised. Blood was collected from the inferior vena cava, heparinized, and centrifuged to obtain the plasma. The samples were dissolved in HNO_3 and evaporated to dryness. The Pt and Gd concentrations were then measured by ICP-MS after the samples were redissolved in 5 N HCl.

***In vivo* MRI of Gd-DTPA/DACHPt–loaded micelles**

MR images were obtained using a 4.7-T UNITY INOVA imaging spectrometer (Varian, Inc.) equipped with a birdcage-type RF coil, 66 mm in diameter. For the T1W of the mice, the following parameters were adopted: spin-echo method, repetition time (TR) = 500 ms, echo time (TE) = 15 ms, field of view (FOV) = 32 × 32 mm^2, matrix size = 256 × 256, and slice thickness = 2 mm. MR images were obtained from C-26 tumor– and BxPC3 tumor–bearing mice when the mean tumor volume was 100 and 400 mm^3, respectively. For all of the mice, transaxial T1W images were taken before injecting Gd-DTPA/DACHPt–loaded micelles as a control. The mice were anesthetized with 1.2% isoflurane during the MRI experiments. The mice were injected i.v. with 5 μmol/kg of Gd-DTPA alone or Gd-DTPA/DACHPt–loaded micelles. The transaxial T1W images were taken with a phantom containing water as a reference signal every 10 minutes for 4 hours. The images were analyzed using Mathematica (Wolfram Research, Inc.) and Excel (Microsoft, Inc.). For each time point, the same level of slices that included the center of the tumors was chosen and segmented by drawing a square that included the tumor area. The pixel intensities in the tissues were compared with the precontrast images and the phantom.

Assessment of therapeutic effect by MRI

MR images were obtained using a 7.0-T MRI scanner (magnet: Kobelco and Jastec; console: Bruker Biospin) with a birdcage-type RF coil, 35 mm in diameter (Rapid Biomedical). The experiment was carried out on BxPC3 tumor–bearing mice at 10 days after implantation when the average size of the tumor was ~60 mm^3. Mice (n = 2) were initially anesthetized with 3.0% isoflurane, orally intubated, and then ventilated with 2.0% isoflurane (Abbott Japan) and 1:2 O_2/room air gas mixture using a rodent ventilator (MRI-1, CWE, Inc.). During MRI scanning, rectal temperature was continuously monitored and maintained at 37.0 ± 0.5°C using a heating pad throughout all scans. T1W MRIs were obtained before and 2 hours after administration of the Gd-DTPA/DACHPt–loaded micelles. The Gd-DTPA/DACHPt–loaded micelles were injected i.v. at 8 mg/kg on a Pt base and 3 mg/kg on a Gd-DTPA base. The control mice were injected i.v. with 30 mg/kg of Gd-DTPA, and they were imaged before and 30 minutes after the injection. The drugs were injected on days 0, 4, 8, 11, and 18. T1W multislice two-dimensional spin echo MRI with fat suppression preparation was obtained with the following parameters: TR = 600 ms (respiratory gating of 100 rpm), TE = 9.5 ms, FOV = 32 × 32 mm^2, matrix size = 256 × 256, slice thickness = 1 mm, and average = 4. Slice orientation of the T1W was transaxial (18 slices, nongap) and horizontal (14 slice, nongap).

Image reconstruction and analysis were performed using ParaVision (version 4.0; Bruker Biospin) and ImageJ (version 1.43; NIH). Regions of interest were identified using a mouse atlas of anatomy, and the volume of the tumors was estimated by the following equation: $V = a \times b^2/2$, where a and b are the major and minor axes of the orthotopic tumors measured from the MR images.

Histology and immunohistochemistry

The excised samples were directly frozen in liquid N_2 for immunohistochemistry or fixed in 4% paraformaldehyde and then paraffin embedded to prepare them for H&E staining. Frozen samples were sectioned at 16-μm thickness in a cryostat, fixed in acetone, and incubated with protein blocking solution (Blocking One Buffer, Nakalai Tesque, Inc.), PECAM-1 (BD Pharmingen), Alexa Fluor 488 secondary antibody (Invitrogen Molecular Probes), and Hoechst (Sigma-Aldrich). The samples were observed by using a Zeiss LSM510 Meta confocal microscope for immunohistochemistry and an Olympus AX80 microscope for H&E staining.

Micro-synchrotron radiation X-ray fluorescence spectrometry analysis

Mice bearing BxPC3 orthotopic tumors were injected i.v. with doses of 3 mg/kg (on a Pt base) of Gd-DTPA/DACHPt–loaded micelles. Four hours after the injection, the mice were

sacrificed and the tumors were excised, frozen in liquid N_2, sliced at 16 μm using a cryostat, and fixed on a polypropylene sheet. Micro-synchrotron radiation X-ray fluorescence spectrometry (μ-SR-XRF) was performed using beamline 37XU (30) at SPring-8, operated at 8 GeV and ~100 mA. The tissue samples were irradiated with incident X-rays with an energy of 14 keV, a beam spot size of 1.3 × 1.3 μm^2, and an intensity of 10^{12} photons/s. The fluorescence X-rays were measured using a Si solid-state detector in air at room temperature. Each sample was mounted on an *x-y* translation stage. The fluorescence X-ray intensity was normalized by the incident X-ray intensity, I_0, to produce a two-dimensional elemental map.

Results

Characterization of Gd-DTPA/DACHPt–loaded micelles

The core-shell micellar nanocarriers with PEG palisade were prepared by preincubating Gd-DTPA and DACHPt at a 1:1 molar ratio for >10 hours in water and mixing this solution with PEG-*b*-P(Glu) (Fig. 1). The incubation of DACHPt with Gd-DTPA may lead to the formation of carboxylato complexes between DACHPt and the carboxylic groups in the DTPA chelator of Gd-DTPA. Accordingly, the FT-IR spectra of the DACHPt, Gd-DTPA, and Gd-DTPA/DACHPt mixtures incubated for 24 hours (Fig. 2A) indicated the appearance of a peak at 1,650 cm^{-1} in the spectra of the Gd-DTPA/DACHPt mixtures assigned to the Pt-COO coordination bond. Moreover, the optimal mixing ratio and incubation time of Gd-DTPA and DACHPt were determined by relaxivity titration. The r_1 of the Gd-DTPA/DACHPt complexes gradually increased up to 4.6 $mmol/L^{-1}s^{-1}$ at a 1:1 ratio from the initial 3.4 $mmol/L^{-1}s^{-1}$ of Gd-DTPA alone (Supplementary Fig. S1A). At DACHPt/Gd-DTPA ratios higher than 1, the r_1 remained constant. In addition, the r_1 of the Gd-DTPA/DACHPt complex gradually increased until 10 hours after mixing. Moreover, the activated state of DACHPt was found to be necessary for binding to Gd-DTPA because the Gd-DTPA/oxaliplatin mixture revealed no increase in the relaxivity (Supplementary Fig. S1B). During the Gd-DTPA/DACHPt complex formation, the stability of the Gd-DTPA complex was evaluated by using the arsenazo III method (29). Consequently, the absence of Gd^{3+}

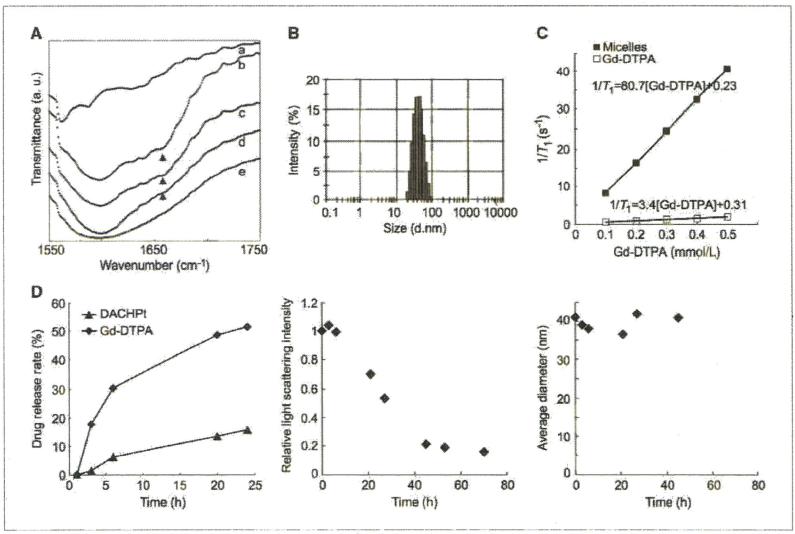

Figure 2. Formation and physicochemical characteristics of Gd-DTPA/DACHPt–loaded micelles. A, FT-IR spectra of DACHPt (a); Gd-DTPA/DACHPt complexes 1:1 (b), 5:1 (c), and 10:1 (d); and Gd-DTPA (e). B, diameter of the micelles determined by DLS. C, longitudinal relaxation ($1/T_1$) of micelles and Gd-DTPA at 37°C. The longitudinal relaxivities (r_1) were calculated from the slope. D, left, release rate of Pt and Gd complexes from Gd-DTPA/DACHPt–loaded micelles in physiologic conditions; middle, relative light scattering intensity of the Gd-DTPA/DACHPt–loaded micelles in physiologic conditions; right, diameter of Gd-DTPA/DACHPt–loaded micelles in physiologic conditions.

in the Gd-DTPA/DACHPt mixture was confirmed (Supplementary Fig. S2).

The obtained micelles were 33 nm in diameter with a narrow size distribution (polydispersity index = 0.067; Fig. 2B). This diameter might be small enough for the micelles to avoid recognition by the reticuloendothelial system, pass through the leaky vasculature of solid tumors by the EPR effect, and attain deep tumor penetration (17). The amounts of DACHPt and Gd-DTPA incorporated in the micelles were found to be 0.42 mg DACHPt/mg polymer and 0.04 mg Gd-DTPA/mg polymer, corresponding to 45% and 5% of the carboxylic groups in PEG-*b*-P(Glu), respectively. Moreover, the r_1 of the micelles increased up to 80.7 $mmol/L^{-1}s^{-1}$, that is, ~24-fold greater than Gd-DTPA alone (Fig. 2C).

The Gd-DTPA/DACHPt–loaded micelles did not release their contents in distilled water (data not shown). However, under physiologic conditions (i.e., 10 mmol/L PBS at 37°C), DACHPt and Gd-DTPA were released in a sustained manner (Fig. 2D, left). Moreover, the release of Gd-DTPA was considerably faster than that of DACHPt, probably due to stronger binding between polymer and DACHPt than between DACHPt and Gd-DTPA. In addition, the safe Gd-DTPA chelates in this system might remain stable because no free Gd^{3+} was detected in the released sample (Supplementary Fig. S3). The gradual drug release from Gd-DTPA/DACHPt–loaded micelles led to a reduction in the light scattering intensity of the micelles (Fig. 2D, middle) due to the decreased density of the micellar cores. Accordingly, the light scattering intensity of the Gd-DTPA/DACHPt–loaded micelles under physiologic conditions decreased to 20% in ~60 hours (Fig. 2D, middle); however, the hydrodynamic diameter of the micelles was maintained at ~30 nm for >48 hours (Fig. 2D, right). The high stability of the micelles and preservation of their hydrodynamic diameter are advantageous in the *in vivo* situation because the structural stability of micelles is highly associated with their prolonged blood circulation (11).

In vivo performance of Gd-DTPA/DACHPt–loaded micelles

The Gd-DTPA/DACHPt–loaded micelles extended the circulation of their cargo in the bloodstream, attaining ~20% of the injected dose of DACHPt after 24 hours and >8% of the injected dose of Gd-DTPA after 4 hours, whereas free oxaliplatin and free Gd-DTPA were rapidly cleared from plasma (Fig. 3A). Moreover, the micelles delivered the drugs to solid tumors due to the increased accumulation and retention at the cancer site because of the EPR effect. Accordingly, the micelles augmented the tumor accumulation 27.7 times for the Pt drug at 24 hours, and >100 times for Gd-DTPA at 4 hours, in subcutaneous murine colon adenocarcinoma 26 (C-26) tumors (Fig. 3B) compared with oxaliplatin and free Gd-DTPA, resulting in high MRI contrast enhancement of the tumor tissue (Fig. 3C). From the ratio of the signal intensities of tumor to muscle, the micelles showed to increase the contrast, whereas the enhancement for Gd-DTPA was almost unchanged. Moreover, the elevated tumor accumulation of Gd-DTPA/DACHPt–loaded micelles may also improve the antitumor activity of the incorporated Pt drug because DACHPt complexes can exert their cytotoxicity after being released from the Gd-DTPA/DACHPt–loaded micelles, as observed in *in vitro* studies (Supplementary Table S1). Accordingly, the micelles showed strong antitumor effect against the C-26 tumor model (Supplementary Fig. S4). Thus, we tested the potential of Gd-DTPA–loaded micelles for monitoring the drug distribution, tumor imaging, and treatment in a pancreatic tumor model close to the clinical situation (i.e., orthotopically inoculated BxPC3 human pancreatic ductal adenocarcinoma tumor).

Direct detection and treatment of pancreatic cancer

The T1W T_1-weighted MR images after i.v. administration of the Gd-DTPA/DACHPt–loaded micelles clearly showed specific contrast enhancement at the tumor area for >4 hours (Fig. 4A and B). In contrast, we did not observe any enhancement in the tumor region after the administration of free Gd-DTPA (Fig. 4A and B), and the signal intensity was higher in the liver, kidney, or spleen than in tumor as suggested from the tumor-to-organ ratios of the MR intensity (Supplementary Table S2). Also, the signals in all organs decreased after 1 hour. The macroscopic observation of the orthotopic tumor-bearing mice that received Gd-DTPA/DACHPt–loaded micelles confirmed the position of every organ and the tumor (Fig. 4D, left and middle), whereas the histologic study of the malignancy revealed the poorly differentiated histology of pancreatic adenocarcinoma, with thick fibrosis and low vascularization (Fig. 4D, right). The amount of Gd-DTPA delivered by the micelles in the orthotopic pancreatic tumor was seven times higher than the accumulation of free Gd-DTPA (Fig. 4C). Accordingly, 3.5% of the total Gd dose from the micelles and 7.2% of the total Pt dose had accumulated within 4 hours of administration.

The antitumor activity of Gd-DTPA/DACHPt–loaded micelles was also evaluated by MRI. Thus, the mice treated with the micelles at 8 mg/kg on a Pt base achieved a significant reduction in the volume of orthotopic BxPC3 tumors (Fig. 5A). Likewise, the weight of the pancreas at day 18 of the micelle-treated animal was much lower than the mice that received only Gd-DTPA (Fig. 5B). Moreover, Gd-DTPA/DACHPt–loaded micelles were shown to enhance the signal intensity at the tumor region (Fig. 5C). Thus, Gd-DTPA/DACHPt–loaded micelle can be used to follow the micelle accumulation in the tumor and the tumor size by MRI, supporting the theranostic concept.

The microdistribution of the drugs at the tumor site was studied using μ-SR-XRF on the pancreatic lesions. Besides the elements traditionally present in animal tissue, such as S, Cl, K, Ca, Fe, Cu, Ni, and Zn, very distinct Pt-L and Gd-L peaks can also be observed in the sum spectrum of the line scan. Thus, the distribution of several atoms (Fe, K, Gd, and Pt) in the tissue sections of the whole pancreas was studied to evaluate the tissue properties and layout of the drugs. The elemental mapping of Fe presents areas with high concentration probably involving the vicinity of blood vessels and the